Turkish Journal of Medical Sciences

Manuscript 5888

Production and characterization of Zn- and Cu-doped Y2O3–Al2O3–SiO2 (YAS) glass microspheres

FATMA UNAL

BATUR ERCAN

Turkish Journal of Medical Sciences

http://journals.tubitak.gov.tr/medical/

Research Article

Turk J Med Sci
(2024) 54: 1092-1101

doi:10.55730/1300-0144.5888

Production and characterization of Zn- and Cu-doped Y2O3–Al2O3–SiO2 (YAS) glass microspheres

Fatma ÜNAL[1,2,3,4,*], **Batur ERCAN**[4,5,6]

[1]Department of Biomedical Engineering, Faculty of Engineering and Natural Sciences, Samsun University, Samsun, Turkiye
[2]Vocational School of Technical Sciences, Samsun University, Samsun, Turkiye
[3]Department of Metallurgical and Materials Engineering, Faculty of Engineering, Hitit University, Çorum, Turkiye
[4]Department of Metallurgical and Materials Engineering, Faculty of Engineering, Middle East Technical University, Ankara, Turkiye
[5]BIOMATEN, Center of Excellence in Biomaterials and Tissue Engineering, Middle East Technical University, Ankara, Turkiye
[6]Biomedical Engineering Program, Middle East Technical University, Ankara, Turkiye

Received: 05.12.2023 • **Accepted/Published Online:** 08.09.2024 • **Final Version:** 18.10.2024

Background/aim: Y_2O_3–Al_2O_3–SiO_2 (YAS) glass microspheres are currently used in radioembolization treatment. However, abscess formation can occur following this treatment. This study aims to endow YAS glass microspheres with antibacterial properties to address the abscesses forming in patients after radioembolization treatment.
Materials and methods: In this study, undoped YAS glass microspheres and those doped with antibacterial agents zinc (Zn) and/or copper (Cu) were successfully fabricated using a sol-gel derived method.
Results: After heat treatment, the microspheres exhibited an amorphous structure. Additionally, the incorporation of Zn and/or Cu dopants did not alter the patterns observed in the X-ray diffraction analysis. Fourier transform infrared spectroscopy analysis detected Si–O–Si, Al–O–Al, and Y–O band vibrations within the structure. The presence of Zn and Cu dopants was confirmed through X-ray photoelectron spectroscopy analysis. Scanning electron microscopy revealed that all samples possessed a regular microsphere morphology, with average particle sizes ranging from 6 to 50 µm. These average particle sizes were further confirmed using a mastersizer.
Conclusion: The antibacterial agent-doped YAS glass microspheres show promise in combating infections that occur following radioembolization treatment.

Key words: Yttrium aluminum silicate, glass microspheres, sol-gel derived method, radioembolization

Graphical abstract

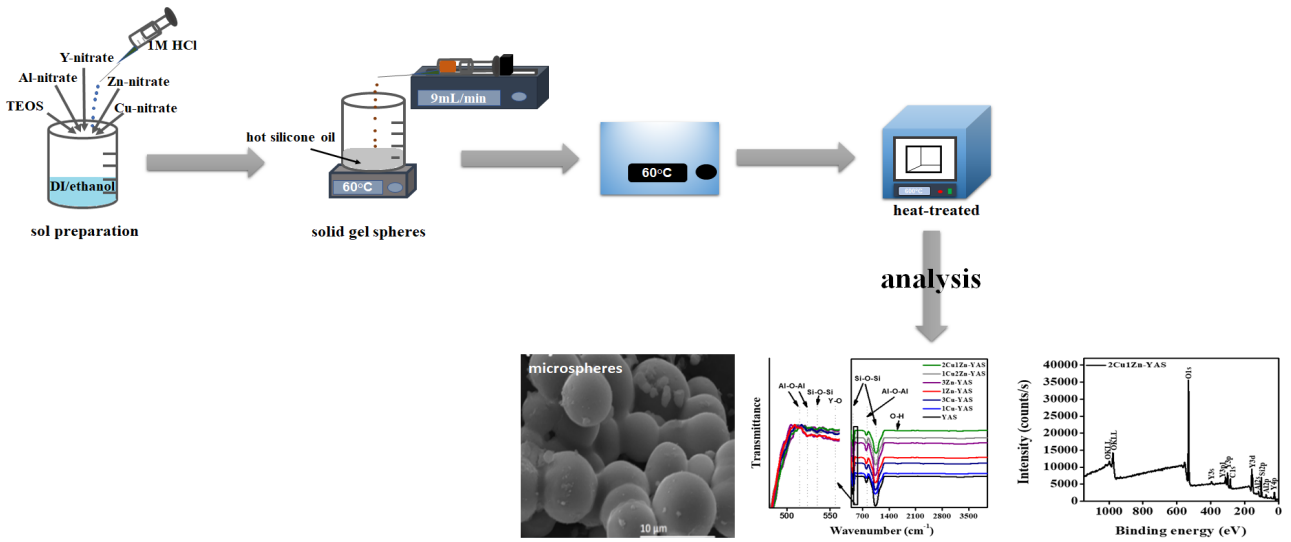

* Correspondence: fatma.unal@samsun.edu.tr

1. Introduction

Surgical intervention is a commonly employed approach for treating cancer. However, postsurgical recovery of the dissected organ may not be complete, which poses a significant concern, particularly when the removed tissue is from a vital organ such as the liver. To address this issue, a minimally invasive radioembolization technique designed only to target and destroy cancerous cells was developed in the mid-1980s [1–5]. This method uses radioactive yttrium aluminum silicate (Y_2O_3–Al_2O_3–SiO_2; YAS) microspheres to treat malignant tumors located deep in the body. Compared to surgical intervention, this technique offers several advantages: it requires minimal medical equipment, is noninvasive, and results in faster patient recovery. The procedure involves placing thousands of tiny radioactive YAS microspheres into the arteries that supply blood to the tumor. Once implanted, these microspheres become lodged in the capillary bed of the tumors, allowing for localized irradiation of the cancerous tissue [6–11]. This targeted approach confines irradiation primarily to cancerous cells, minimizing damage to surrounding healthy tissue. The potential use of $17Y_2O_3$–$19Al_2O_3$–$64SiO_2$ (mol%) ceramic microspheres for in situ irradiation of cancers via radioembolization was first reported by Hyatt and Day in 1987 [1]. Subsequent research on this topic was continued by Erbe and Day in 1993 [2]. Today, these ceramic microspheres are widely used in clinics worldwide, saving thousands of lives each year.

Although YAS glass microspheres are currently utilized in radiation oncology, abscess formation following cancer treatment remains contentious. This complication can lead to inflammation, bacterial contamination, and infection. Attasi et al. reported that abscess formation occurred in 98 of 327 patients with hepatocellular carcinoma (190) or liver metastases (137) after undergoing radioembolization therapy [12]. Mascarenhas et al. treated a 58-year-old woman with a gastrin-secreting cell tumor using yttrium-90 radioembolization. Following the treatment, *Escherichia coli* (*E. coli*) bacteria were detected in the patient, prompting the administration of antibiotic therapy [13]. Korkmaz et al. administered radioembolization treatment to a 53-year-old female patient with pancreatic cancer. Unfortunately, the *E. coli* infection that occurred posttreatment led to abscess formation and resulted in the patient's death [14]. Similarly, Kurilova et al. treated 10 patients with ^{90}Y glass microspheres and observed liver abscesses following the treatment [15]. Wong et al. also reported abscess formation after treating liver metastases [16].

In the event of infection, the primary treatment method has traditionally been using antibiotics. However, antibiotic treatment for bacterial biofilms has proven less effective, and bacteria have progressively developed resistance to commonly used antibiotics, such as Methicillin-resistant *Staphylococcus aureus*. This escalating resistance further complicates the fight against infections. Infection remains a significant clinical challenge, prompting extensive research to mitigate or eliminate infection-related risks. It is well-established that employing materials with unique antibacterial properties can reduce infection risk. Additionally, methods such as ion release have been shown to inhibit bacterial resistance and contribute to infection control [17].

Antimicrobial agent-doped materials, including those containing copper (Cu), zinc (Zn), Mg, Ag, Se, and Sr, have been employed in combating bacterial infections [18–25]. Zn and Cu, which are essential trace elements for humans [26–28], are currently utilized in clinical biomedical applications [29–31] due to their antibacterial properties and biocompatibility [18,26,28,32,33]. Unal et al. reported that Zn-doped 58S bioglass effectively inhibited the growth of *S. aureus* and *E. coli* bacteria [19]. Kumar et al. documented the antibacterial activity of Zn-doped S53P4 glass against *E. coli* and *S. aureus* [34]. Additionally, Sánchez-Salcedo et al. observed that Zn-doped bioglass demonstrated antibacterial behavior, specifically against *S. aureus* [35]. Hosseini et al. reported that Cu-doped mesoporous bioactive glasses exhibited antibacterial properties against Methicillin-resistant *S. aureus* bacteria [36]. Bari et al. found that Cu-doped mesoporous bioactive glasses showed antibacterial effects against *E. coli*, *S. aureus* and *Staphylococcus epidermidis* (*S. epidermidis*) [21]. Alasvand et al. documented that Cu-doped glass effectively inhibited the survival of *S. aureus* and *Pseudomonas aeruginosa* (*P. aeruginosa*) bacteria [37]. While numerous studies have explored the antibacterial properties of materials doped with Zn and Cu, research specifically addressing Cu and Zn doping of YAS microspheres is lacking. Therefore, this study aims to synthesize, for the first time, Zn- and Cu-doped YAS microspheres using a sol-gel-derived method. By capitalizing on the antibacterial properties of YAS, the study aims to prevent infection formation in patients, thereby potentially reducing or eliminating the need for antibiotic treatment.

2. Materials and methods

2.1. Production of YAS glass microspheres

Yttrium (III) nitrate hexahydrate ($Y(NO_3)_3.6H_2O$), tetraethyl orthosilicate ($C_8H_{20}O_4Si$), and copper (II) nitrate trihydrate ($Cu(NO_3)_2{\cdot}3H_2O$) were obtained from Acros (Acros Organics, Geel, Belgium). Aluminum nitrate nonahydrate ($Al(NO_3)_3{\cdot}9H_2O$) and zinc nitrate hexahydrate ($Zn(NO_3)_2{\cdot}6H_2O$) were acquired from Sigma-Aldrich (Sigma-Aldrich Corp., St. Louis, MO, USA).

Hydrochloric acid (HCl, 37%) was supplied by Merck (Merck, Rahway, NY, USA). The synthesis of the glass microspheres involved two steps: a) sol preparation and b) microsphere formation. The resulting microspheres had the following composition range: 17 mol% Y_2O_3, 64 mol% SiO_2, 16–19 mol% Al_2O_3, 1–3 mol% CuO, and 1–3 mol% ZnO. The detailed chemical compositions of the microspheres are presented in Table 1.

a) Sol preparation

For sol preparation, tetraethyl orthosilicate (TEOS) was introduced into a distilled water/ethanol solution (volume ratio of 2:1) and mixed at 300 rpm to facilitate the hydrolysis and polycondensation of TEOS. Based on the desired composition of the microspheres, aluminum nitrate (Al-nitrate), yttrium nitrate (Y-nitrate), copper nitrate (Cu-nitrate), and zinc nitrate (Zn-nitrate) salts were sequentially added to the prepared TEOS solution at 20-min intervals, with continued mixing at 300 rpm. Subsequently, a 1M HCl solution was added to induce sol formation, and the mixture was stirred for 1 h following the formation of the sol.

b) Formation of the microspheres

The obtained sol was loaded into a 21G needle syringe and injected into hot silicone oil (approximately 60 °C) at a 9-mL/min flow rate using a syringe pump under magnetic stirring. After injection, the solid gel spheres were separated from the hot oil using hot water, followed by rinsing with petroleum ether and distilled water to ensure complete oil removal. The separated microspheres were then dried at 60 °C for 24 h. Finally, the microspheres were heat-treated at 600 °C for 5 h at a heating rate of 3 °C/min

2.2. Characterization of the microspheres

Structural analyses of the synthesized microspheres were conducted using X-ray diffraction (XRD) analysis at a scan speed of 1°/min over the 2θ range of 10–90°, employing a Rigaku X-Ray Diffractometer (Rigaku, Tokyo, Japan). To elucidate the molecular bond properties of the microspheres, Fourier transform infrared spectroscopy (FT-IR) measurements were performed in the 4000–400 cm^{-1} wavenumber range using a Hyperion 1000 IR microscope device in ATR mode (Bruker Optik Gmbh, Ettlingen, Germany). The elemental composition of the microspheres was analyzed by X-ray photoelectron spectroscopy (XPS) using a PHI 5000 Versaprobe instrument, with binding energy (BE) calibrated against the C1s reference peak at 284.80 eV. Morphological analysis was carried out through scanning electron microscopy (SEM) using a Nova Nano SEM 430 (FEI Company). For SEM analysis, the microspheres were mounted on an aluminum holder and coated with a gold-palladium alloy using a Quorum SC7640 high-resolution sputter coater (Quorum Technologies, East Sussex, UK). The particle sizes of the microspheres were determined using a Malvern Mastersizer 2000 (Malvern Panalytical, Malvern, UK), and the specific surface area was measured with a Quantachrome Autosorb-6 surface area analyzer (Anton Paar Quantatech, Boyton Beach, FL, USA). The measurements were based on a liquid dispersion with a refractive index of 1.658.

3. Results

3.1. Structural analysis

The XRD patterns of all the microspheres are presented in Figure 1. The microspheres displayed an amorphous structure, characterized by an amorphous hump observed between approximately 2θ = 15° and 40° for all powders. Additionally, incorporating Zn and/or Cu dopant elements did not alter the XRD patterns, indicating that the dopants did not influence the crystallization process.

3.2. Chemical analysis

The FT-IR spectra of the YAS, 1Cu-YAS, 1Zn-YAS, 3Cu-YAS, 3Zn-YAS, 1Cu2Zn-YAS, and 2Cu1Zn-YAS microsphere samples are presented in Figure 2. The observed peaks confirm the successful synthesis of the YAS chemistry. The peak around 454 cm^{-1} is attributed to the Si-O-Si bending vibration [38], while the peaks around 535 and 1080 cm^{-1} are associated with the Si–O–Si vibration [39,40]. The peak at approximately 515 cm^{-1} corresponds to the aluminum oxide stress mode [41]. The peaks around 524 and 807 cm^{-1} are assigned to Al-O-Al

Table 1. Chemical compositions of the YAS glass microspheres.

Designation	Chemical composition (mol%)				
	Y_2O_3	SiO_2	Al_2O_3	CuO	ZnO
YAS	17	64	19	0	0
1Cu-YAS	17	64	18	1	0
3Cu-YAS	17	64	16	3	0
1Zn-YAS	17	64	18	0	1
3Zn-YAS	17	64	16	0	3
1Cu2Zn-YAS	17	64	16	1	2
2Cu1Zn-YAS	17	64	16	2	1

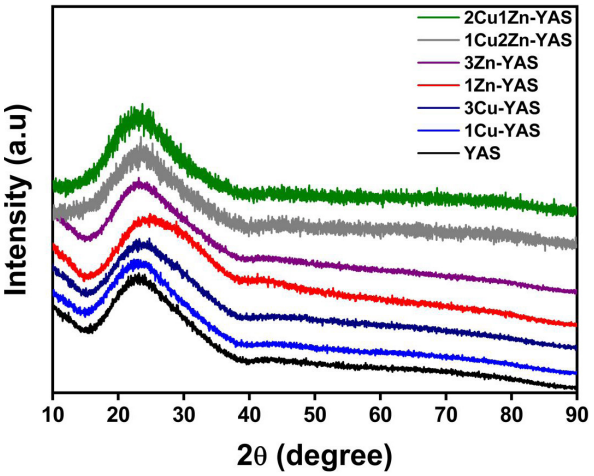

Figure 1. XRD patterns of the YAS, 1Cu-YAS, 3Cu-YAS, 1Zn-YAS, 3Zn-YAS, 1Cu2Zn-YAS, and 2Cu1Zn-YAS microsphere samples.

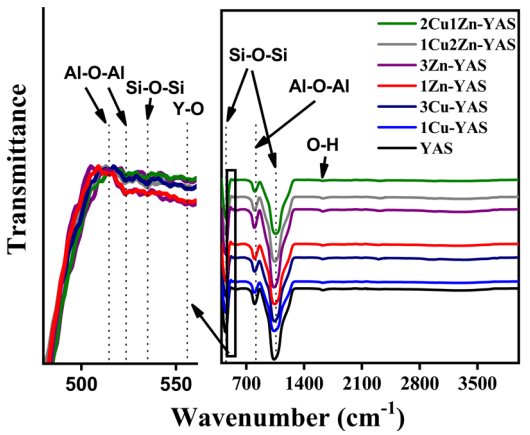

Figure 2. FT-IR spectra of the YAS, 1Cu-YAS, 3Cu-YAS, 1Zn-YAS, 3Zn-YAS, 1Cu2Zn-YAS, and 2Cu1Zn-YAS microsphere samples.

vibrations [42,43], and the peak at approximately 557 cm^{-1} indicates the vibrations in the Y–O bonds [44]. The peak around 1627 cm^{-1} was attributed to the bending mode of adsorbed water molecules [40,45]. The band assignments from the FT-IR data are detailed in Table 2. The bond vibrations of Zn- and Cu-doped elements could not be detected by FT-IR analysis due to their low concentration in the structure. Therefore, XPS analysis was conducted to confirm the presence of Zn and Cu dopant elements in the microspheres.

The elemental composition of the 2Cu1Zn-YAS microspheres was analyzed using XPS. The XPS wide-scan spectrum is shown in Figure 3a and confirms the presence of Si, Al, Y, and O elements. Since the dopant elements were not visible in the general spectrum, high-resolution scans were conducted to verify the presence of these dopants (Figure 3b–f). The high-resolution XPS spectrum for Y3d (Figure 3b) revealed BEs of $Y3d_{3/2}$ at 159.70 eV and $Y3d_{5/2}$ at 157.61 eV [46–48]. The XPS spectrum for Al2p showed BEs of $Al2p_{1/2}$ at 73.4 eV and 76.2 eV and $Al2p_{3/2}$ at 72.3 eV and 74.4 eV (Figure 3c) [49–51]. The XPS spectrum for Si2p exhibited a BE of 102.1 eV, as illustrated in Figure 3d [52]. The high-resolution XPS spectrum for Zn2p (Figure 3e) revealed BEs for $Zn2p_{3/2}$ and $Zn2p_{1/2}$ centered at approximately 1021.9 eV and 1044.9 eV, respectively [53,54]. The high-resolution XPS spectrum of Cu2p (Figure 3f) indicated BEs of 932.2 eV and 952.6 eV for $Cu2p_{3/2}$ and $Cu2p_{1/2}$, respectively [55,56]. Consequently, the XPS analysis confirmed the incorporation of Zn and Cu dopant elements into the structure. The spectral lines and BEs are summarized in Table 3.

Table 2. FT-IR spectra band assignment for the glass microspheres.

Band assignment	Wavenumber (cm^{-1})	References
Si-O-Si bending vibration	454	[38]
Si–O–Si vibration	535 and 1080	[39,40]
Aluminum oxide stress mode	515	[41]
Al-O-Al vibration	524 and 807	[42,43]
Y–O vibration	557	[44]
Adsorbed water molecules bending mode	1627	[40,45]

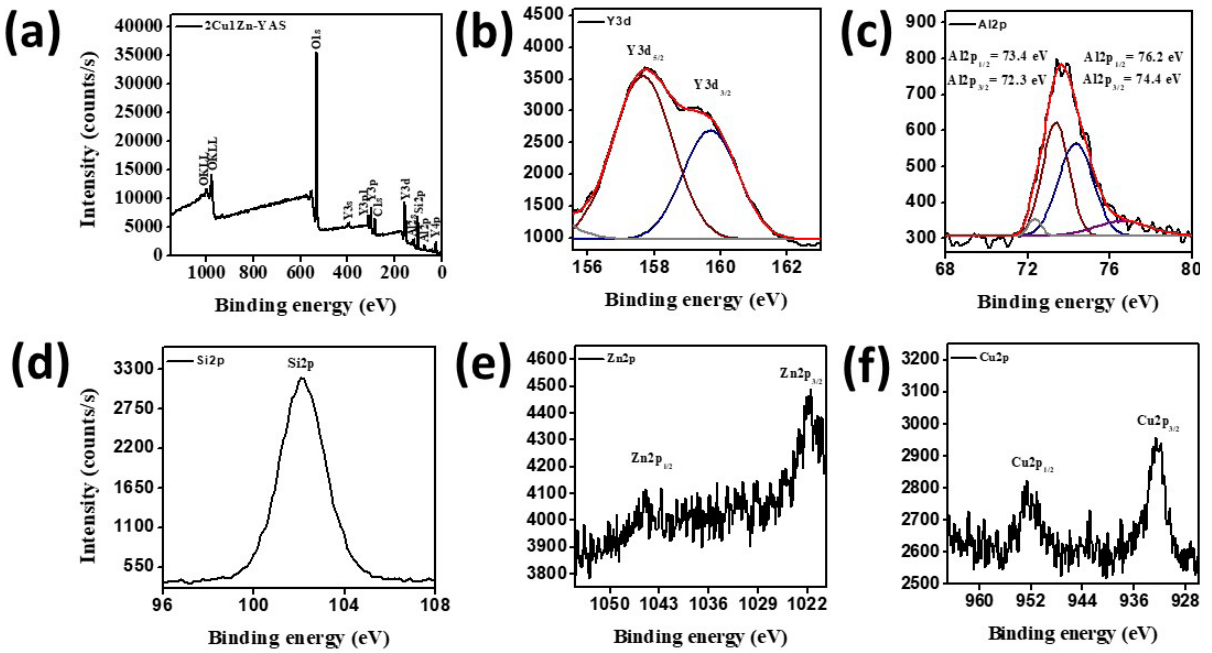

Figure 3. XPS (a) wide spectrum and high resolution (b) Y3d, (c) Al2p, (d) Si2p, (e) Zn2p, and (f) Cu2p spectra of the 2Cu1Zn-YAS microsphere sample.

Table 3. XPS data in terms of spectral line and binding energy.

Element	Spectral line	Energy (eV)	References
Y	3d3/2	159.70	[46–48]
Y	3d5/2	157.61	[46–48]
Al	2p1/2	73.4 and 76.2	[49–51]
Al	2p3/2	72.3 and 74.4	[49–51]
Si	2p	102.1	[52]
Zn	2p3/2	1021.9	[53]
Zn	2p1/2	1044.9	[54]
Cu	2p3/2	932.2	[55]
Cu	2p1/2	952.6	[56]

3.3. Morphological analysis

SEM images of the YAS, 1Cu-YAS, 3Cu-YAS, 1Zn-YAS, 3Zn-YAS, 1Cu2Zn-YAS, and 2Cu1Zn-YAS samples are shown in Figure 4a–g. The images revealed that all microsphere samples exhibited a regular spherical shape. However, the particles displayed an agglomerated morphology, with particles adhering to one another. The average particle size ranged from 6 to 50 μm, depending on the type and amount of the dopant used. These particle size measurements were also obtained using the mastersizer method and are detailed in Table 4.

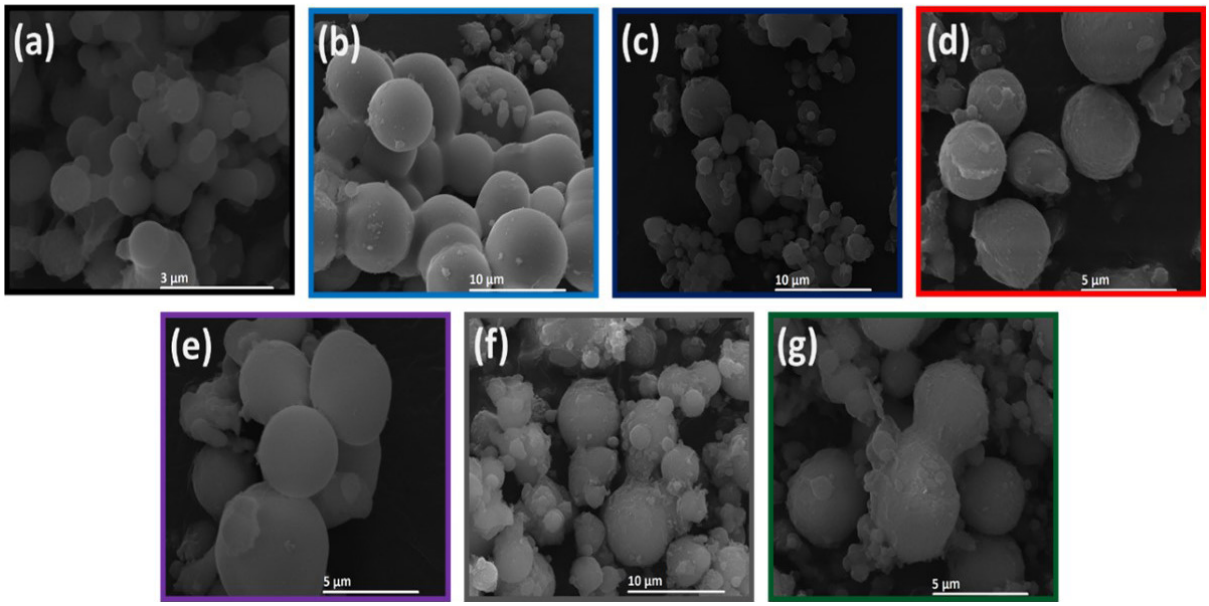

Figure 4. SEM images of the (a) YAS, (b) 1Cu-YAS, (c) 3Cu-YAS, (d) 1Zn-YAS, (e) 3Zn-YAS, (f) 1Cu2Zn-YAS, and (g) 2Cu1Zn-YAS microsphere samples.

Table 4. Average sizes and specific surface areas of the samples.

Designation	$d_{(0.9)}$, (µm)	Specific surface area (m^2/g)
YAS	23.53	1.25
1Cu-YAS	35.11	0.98
1Zn-YAS	48.49	0.80
3Cu-YAS	12.90	1.39
3Zn-YAS	29.64	1.04
1Cu2Zn-YAS	53.03	0.97
2Cu1Zn-YAS	51.18	0.94

3.4. Particle size measurement

Table 4 provides the average particle size and specific surface area values for the YAS, 1Cu-YAS, 1Zn-YAS, 3Cu-YAS, 3Zn-YAS, 1Cu2Zn-YAS, and 2Cu1Zn-YAS glass microspheres. It was observed that the average particle size depends on the type and amount of dopant used. The variation in particle size can be attributed to the sol stage, where the silica network (-Si–O–Si-) is formed through the polycondensation of Si–OH groups. This network is subsequently modified by adding Y-nitrate, Al-nitrate, Cu-nitrate, and Zn-nitrate salts, influencing the final particle size. Thus, the replacement of Y with Zn or Cu on a molar basis after adding Zn- or Cu-nitrate salts resulted in a narrower silica network due to the smaller ionic radii of Cu (0.071 nm) and Zn (0.074 nm) compared to Y (0.090 nm). This narrower network led to a reduction in particle size [57–59]. Additionally, the specific surface area values ranged from 0.80 to 1.39 m^2/g.

4. Discussion

The comprehensive analysis of the microspheres, including XRD, FT-IR, XPS, and SEM, provides a detailed understanding of their structural and compositional characteristics. XRD patterns, shown in Figure 1, confirm that all microsphere samples exhibit an amorphous structure, with no significant changes due to the incorporation of Zn and/or Cu dopants, indicating that the dopants did not affect crystallization. Similarly, Unal et al. [19] found that adding dopant elements did not result in any changes in the XRD peaks, further confirming the amorphous nature of the structure, as indicated by the XRD peaks. FT-IR spectra (Figure 2) validate the successful synthesis of YAS, with key peaks attributed to Si-O-Si bending vibrations, Si–O–Si vibrations, and various metal-oxide bond vibrations. Peaks at approximately 1627 cm^{-1} indicate adsorbed water. The bond vibrations of the Zn and Cu dopants could not be detected by

FT-IR, necessitating XPS analysis, which confirmed the presence of these dopants. High-resolution XPS spectra (Figure 3b–f) revealed BEs consistent with Y, Al, Si, Zn, and Cu, validating the incorporation of Zn and Cu into the microspheres. SEM images (Figure 4) show that all samples maintain a spherical shape but exhibit an agglomerated morphology, similar to the findings of Ghahramani et al. [4], who synthesized spherical particles with an agglomerated morphology in their study. Particle sizes, ranging from 6 to 50 μm, and specific surface areas (0.80 to 1.39 m^2/g) vary with the dopant type and amount, attributed to modifying the silica network by dopants. Replacing Y with Zn or Cu narrows the silica network, leading to smaller particle sizes. This integrated analysis underscores the successful synthesis and structural modifications of the microspheres, highlighting their potential for further applications in various fields.

5. Conclusion

(1) Zn- and Cu-doped YAS glass microspheres were synthesized using a sol-gel-derived method in two stages. Initially, a sol was prepared and introduced into hot silicone oil with a syringe. The resulting solid gel spheres were subsequently dried and heat-treated at 600 °C for 5 h. XRD analysis confirmed that the microspheres possessed an amorphous structure and that the dopant elements did not influence the crystallization process.

(2) FT-IR analysis identified Si–O–Si, Al–O–Al, and Y–O vibrations, confirming the presence of Y, Al, Si, and O in the microsphere structure. XPS analysis confirmed the successful incorporation of Cu and Zn into the YAS glass microspheres. Morphological analysis revealed an agglomerated spherical morphology. SEM analysis and particle-size measurements indicated that the average particle size ranged from 6 to 50 μm. Additionally, the specific surface areas of the microspheres varied between 0.80 and 1.39 m^2/g.

(3) Given that the particle size of YAS microspheres used in clinical practice ranges between 15 and 35 μm, our study identified that the 1Cu-YAS and 3Zn-YAS samples demonstrated optimal dopant amounts and types for use in radioembolization therapy. These antibacterial microspheres show promise in combating infections that may occur following radioembolization treatment.

Acknowledgments/disclaimers/conflict of interest

This work was supported by Hitit University's Scientific Research Project, Türkiye (grant no. MUH19001.20.011).

The authors declare that they have no conflict of interest.

References

1. Hyat MJ, Day DE. Glass properties in the yttria-alumina-silica system. Journal of the American Ceramic Society 1987; 70 (10): C283-287. https://doi.org/10.1111/j.1151-2916.1987.tb04901.x
2. Ehrhardt GJ, Day DE. Therapeutic use of 90Y microspheres. International Journal of Radiation Applications and Instrumentation. Part B Nuclear Medicine and Biology 1987; 14 (3): 233-242. https://doi.org/10.1016/0883-2897(87)90047-x
3. Erbe EM, Dayt DE. Chemical durability of Y203-Al203-Si02 glasses for the in vivo delivery of beta radiation. Journal of Biomedical Materials Research 1993; 27 (10):1301-1308. https://doi.org/10.1002/jbm.820271010
4. Ghahramani MR, Garibov AA, Agayev TN, Mohammadi MA. A novel way to production yttrium glass microspheres for medical applications. Glass Physics and Chemistry 2014; 40 (3):283-287. https://doi:10.1134/S1087659614030055
5. Kawashita M. Ceramic microspheres for biomedical applications. International Journal of Applied Ceramic Technology 2005; 2 (3):173-183. https://doi.org/10.1111/j.1744-7402.2005.02023.x
6. Nosrati Z, Khanchi AR, Sheybani S. Preparation of low-density 90Y microspheres consisting of mesoporous silica core/yttria shell: A potential therapeutic agent for hepatic tumors. Journal of Radioanalytical and Nuclear Chemistry 2014; 301: 373-382. https://doi.org/10.1007/s10967-014-3168-0
7. Murthy R, Nunez R, Szklaruk J, Erwin W, Madoff DC, Gupta S, Ahrar K, Wallace M, Cohen A, Coldwell DM, Kennedy AS, Hicks ME. Yttrium-90 microsphere therapy for hepatic malignancy: Devices, indications, technical considerations, and potential complications. Radiographics. 2005; 25: 41-56. https://doi.org/10.1148/rg.25si055515
8. Garrean S, Espat JN. Yttrium-90 internal radiation therapy for hepatic malignancy. Surgical Oncology 2005; 14: 179-193. https://doi.org/10.1016/j.suronc.2006.01.003
9. Meram E, Longhurst C, Vardar BU, Karaoglu K, Laeseke PF, Ozkan OS. Evaluation of staging systems to predict prognosis in hepatocellular carcinoma patients treated with radioembolization. Heliyon. 2022; 8: e08770. https://doi.org/10.1016/j.heliyon.2022.e08770

10. Cholapranee A, van Houten D, Deitrick G, Dagli M, Sudheendra D, Mondschein JI, Soulen MC. Risk of liver abscess formation in patients with prior biliary intervention following yttrium-90 radioembolization. CardioVascular and Interventional Radiology 2015; 38(2): 397-400. https://doi.org/10.1007/s00270-014-0947-5

11. Saini A, Wallace A, Alzubaidi S, Knuttinen MG, Naidu S, Sheth R, Albadawi H, Oklu R. History and evolution of yttrium-90 radioembolization for hepatocellular carcinoma. Journal of Clinical Medicine 2019; 8: 55. https://doi.org/10.3390/jcm8010055

12. Atassi B, Bangash AK, Lewandowski RJ, Ibrahim S, Kulik L, Mulcahy MF, Murthy R, Ryu RK, Sato KT, Miller FH, Omary RA, Salem R. Biliary sequelae following radioembolization with yttrium-90 microspheres. Journal of Vascular and Interventional Radiology 2008; 19: 691-697. https://doi.org/10.1016/j.jvir.2008.01.003

13. Mascarenhas NB, Mulcahy MF, Lewandowski RJ, Salem R, Ryu RK. Hepatic abscess after yttrium-90 radioembolization for islet-cell tumor hepatic metastasis. CardioVascular and Interventional Radiology 2010; 33: 650-653. https://doi.org/10.1007/s00270-009-9617-4

14. Korkmaz M, Bozkaya H, Çinar C, Şanal B, Güneyli S, Parıldar M, Oran I. Liver abscess following radioembolization with yttrium-90 microspheres. Wiener klinische Wochenschrift 2014; 126: 785-788. https://doi.org/10.1007/s00508-014-0609-2

15. Kurilova I, Bendet A, Fung EK, Petre EN, Humm JL, Boas FE, Crane CH, Kemeny N, Kingham TP, Cercek A, D'Angelica MI, Beets-Tan RGH, Sofocleous CT. Radiation segmentectomy of hepatic metastases with Y-90 glass microspheres. Abdominal Radiology 2021;46:3428-3436. https://doi.org/10.1007/s00261-021-02956-6

16. Wong TY, Zhang KS, Gandhi RT, Collins ZS, O'Hara R, Wang EA, Vaheesan K, Matsuoka L, Sze DY, Kennedy AS, Brown DB. Long-term outcomes following 90Y Radioembolization of neuroendocrine liver metastases: evaluation of the radiation-emitting SIR-spheres in non-resectable liver tumor (RESiN) registry. BMC Cancer. 2022; 22: 224. https://doi.org/10.1186/s12885-022-09302-z

17. Zheng K, Balasubramanian P, Paterson TE, Stein R, MacNeil S, Fiorilli S, Vitale-Brovarone C, Shepherd J, Boccaccini AR. Ag modified mesoporous bioactive glass nanoparticles for enhanced antibacterial activity in 3D infected skin model. Materials Science &Engineering C 2019; 103 :109764. https://doi.org/10.1016/j.msec.2019.109764

18. Jacobs A, Renaudin G, Forestier C, Nedelec JM, Descamps S. Biological properties of copper-doped biomaterials for orthopedic applications: A review of antibacterial, angiogenic and osteogenic aspects. Acta Biomaterialia 2020; 117: 21-39. https://doi.org/10.1016/j.actbio.2020.09.044

19. Unal F, Tasar C, Ercan B. Fabrication and in vitro characterization of antibacterial magneto-luminescent core-shell bioactive glass nanoparticles. Ceramics International 2023;49(12):20118-20126. https://doi.org/10.1016/j.ceramint.2023.03.135

20. Rodríguez-Valencia C, Lopez-Álvarez M, Cochón-Cores B, Pereiro I, Serra J, González P. Novel selenium-doped hydroxyapatite coatings for biomedical applications. Journal of Biomedical Materials Research - Part A 2013; 101 (3): 853-861. https://doi.org/10.1002/jbm.a.34387

21. Bari A, Bloise N, Fiorilli S, Novajra G, Vallet-Regí M, Bruni G, Torres-Pardo A, González-Calbet JM, Visai L, Vitale-Brovarone C. Copper-containing mesoporous bioactive glass nanoparticles as multifunctional agent for bone regeneration. Acta Biomaterialia 2017;55:493-504. https://doi.org/10.1016/j.actbio.2017.04.012

22. Çakmak T, Kaya EE, Küçük D, Ebin B, Balci O, Gürmen S. Novel strategy for one-step production of attenuated Ag-containing AgCu/ZnO antibacterial-antifungal nanocomposite particles. Powder Metallurgy and Metal Ceramics 2020; 59: 261-270. https://doi.org/10.1007/s11106-020-00158-1

23. Moghanian A, Ghorbanoghli A, Kazem-Rostami M, Pazhouheshgar A, Salari E, Yazdi MS, Alimardani T, Jahani H, Jazi FS, Tahriri M. Novel antibacterial Cu/Mg-substituted 58S-bioglass: Synthesis, characterization and investigation of in vitro bioactivity. International Journal of Applied Glass Science 2020; 11: 685-698. https://doi.org/10.1111/ijag.14510

24. Zhang Y, Hu M, Zhang W, Zhang X. Homology of selenium (Se) and tellurium (Te) endow the functional similarity of Se-doped and Te-doped mesoporous bioactive glass nanoparticles in bone tissue engineering. Ceramics International 2022; 48: 3729-3739. https://doi.org/10.1016/j.ceramint.2021.10.155

25. Ranga N, Gahlyan S, Duhan S. Antibacterial efficiency of Zn, Mg and Sr doped bioactive glass for bone tissue engineering. Journal of Nanoscience and Nanotechnology 2020; 20: 2465-2472. https://doi.org/10.1166/jnn.2020.17336

26. Tortella GR, Pieretti JC, Rubilar O, Fernandez-Baldo- M, Benavides-Mendoza A, Diez MC, Seabra AB. Silver, copper and copper oxide nanoparticles in the fight against human viruses: progress and perspectives. Critical Reviews in Biotechnology 2022; 42 (3): 431-449. https://doi.org/10.1080/07388551.2021.1939260

27. Jeejeebhoy K. Zinc: An essential trace element for parenteral nutrition. Gastroenterology 2009; 137 (5): S7-S12. https://doi.org/10.1053/j.gastro.2009.08.014

28. Sirelkhatim A, Mahmud S, Seeni A, Kaus NHM, Ann LC, Bakhori SKM, Hasan H, Mohamad D. Review on zinc oxide nanoparticles: Antibacterial activity and toxicity mechanism. Nano-Micro Letters 2015; 7 (3): 219-242. https://doi.org/10.1007/s40820-015-0040-x

29. Zatcoff RC, Smith MS, Borkow G. Treatment of tinea pedis with socks containing copper-oxide impregnated fibers. The Foot. 2008; 18: 136-141. https://doi.org/10.1016/j.foot.2008.03.005

30. Schmidt MG, Attaway HH, Fairey SE, Steed LL, Michels HT, Salgado CD. Copper continuously limits the concentration of bacteria resident on bed rails within the intensive care unit. Infection Control and Hospital Epidemiology 2013; 34 (5): 530-533. https://doi.org/10.1086/670224

31. Bhatnagar S, Wadhwa N, Aneja S, Lodha R, Kabra SK, Natchu UCM, Sommerfelt H, Dutta AK, Chandra J, Rath B, Sharma M, Sharma VK, Kumari M, Strand TA. Zinc as adjunct treatment in infants aged between 7 and 120 days with probable serious bacterial infection: a randomised, double-blind, placebo-controlled trial. Lancet. 2012; 379: 2072-2078. https://doi.org/10.1016/S0140-6736(12)60477-2

32. Tran CD, Makuvaza J, Munson E, Bennett B. Biocompatible copper oxide nanoparticle composites from cellulose and chitosan: Facile synthesis, unique structure, and antimicrobial activity. ACS Applied Materials and Interfaces. 2017; 9: 42503-42515. https://doi.org/10.1021/acsami.7b11969

33. Ramesh P, Saravanan K, Manogar P, Johnson J, Vinoth E, Mayakannan M. Green synthesis and characterization of biocompatible zinc oxide nanoparticles and evaluation of its antibacterial potential. Sensing and Bio-Sensing Research 2021; 31: 100399. https://doi.org/10.1016/j.sbsr.2021.100399

34. Kumar A, Gajraj V, Das A, Sen D, Xu H, Mariappan CR. Silver, copper, magnesium and zinc contained electroactive mesoporous bioactive S53P4 glass–ceramics nanoparticle for bone regeneration: bioactivity, biocompatibility and antibacterial activity. Journal of Inorganic and Organometallic Polymers and Materials 2022; 32: 2309-2321. https://doi.org/10.1007/s10904-022-02295-z

35. Sánchez-Salcedo S, Heras C, Lozano D, Vallet-Regí M, Salinas AJ. Nanodevices based on mesoporous glass nanoparticles enhanced with zinc and curcumin to fight infection and regenerate bone. Acta Biomaterialia 2023; 166: 655-669. https://doi.org/10.1016/j.actbio.2023.04.046

36. Hosseini M, Besheli HN, Deng D, Lievens C, Zuo Y, Leeuwenburgh SCG, Yang F. Facile post modification synthesis of copper-doped mesoporous bioactive glass with high antibacterial performance to fight bone infection. Biomaterials Advances 2023; 144: 213198. https://doi.org/10.1016/j.bioadv.2022.213198

37. Alasvand N, Behnamghader A, Milan PB, Mozafari M. Synthesis and characterization of novel copper-doped modified bioactive glasses as advanced blood-contacting biomaterials. Materials Today Chemistry 2023; 29: 101465. https://doi.org/10.1016/j.mtchem.2023.101465

38. Azizabadi N, Azar PA, Tehrani MS, Derakhshi P. Synthesis and characteristics of gel-derived SiO2-CaO-P2O5-SrO-Ag2O-ZnO bioactive glass: Bioactivity, biocompatibility, and antibacterial properties. Journal of Non-Crystalline Solids 2021; 556 :120568. https://doi.org/10.1016/j.jnoncrysol.2020.120568

39. El-Nahhal IM, Salem JK, Kuhn S, Hammad T, Hempelmann R, Al Bhaisi S. Synthesis and characterization of silica-, meso-silica- and their functionalized silica-coated copper oxide nanomaterials. Journal of Sol-Gel Science and Technology 2016; 79 (3):573-583. https://doi.org/10.1007/s10971-016-4034-z

40. Khalil KMS. Cerium modified MCM-41 nanocomposite materials via a nonhydrothermal direct method at room temperature. Journal of Colloid and Interface Science 2007; 315: 562-568. https://doi.org/10.1016/j.jcis.2007.07.030

41. Rabu AR, Jewena N. Das SK, Khandaker JI, Ahmed F. Synthesis of metal-oxide (Al2O3) nanoparticles by using autoclave for the efficient absorption of heavy metal ions. Journal of Nanomaterials & Molecular Nanotechnology 2020; 9(6).

42. Gao L, Shi Z, Liu Y, Zhao Y, Liu Q, Xu C, Bai P, Yan Z. Effect of SiO2/Al2O3 ratio on micro-mesopore formation for Pt/Beta-MCM-41 via NaOH treatment and the catalytic performance in n-heptane hydro isomerization. IOP Conference Series: Earth and Environmental Science 2018; 108: 042105. https://doi.org/10.1088/1755-1315/108/4/042105

43. Khodadadi A, Farahmandjou M, Yaghoubi M. Investigation on synthesis and characterization of Fe-doped Al2O3 nanocrystals by new sol–gel precursors. Materials Research Express 2019; 6: 025029. https://doi.org/10.1088/2053-1591/aaef70

44. Zhang L, Li Z, Zhen F, Wang L, Zhang Q, Sun R, Selim FA, Wong C, Chen H. High sinterability nano-Y2O3 powders prepared via decomposition of hydroxyl-carbonate precursors for transparent ceramics. Journal of Materials Science 2017; 52: 8556-8567. https://doi.org/10.1007/s10853-017-1071-0

45. Nayan MB, Jagadish K, Abhilash MR, Namratha K, Srikantaswamy S. Comparative study on the effects of surface area, conduction band and valence band positions on the photocatalytic activity of ZnO-MxOy heterostructures. Journal of Water Resource and Protection 2019; 11: 357-370. https://doi.org/10.4236/jwarp.2019.113021

46. Mariscal-Becerra L, Acosta-Najarro D, Falcony-Guajardo C, Murrieta Sanchez H. Luminescent and structural analysis of yttrium oxide doped with different percentages of terbium and dysprosium, to obtain different shades of green to yellow. Journal of Nanophotonics. 2018; 12 (2): 026018. https://doi.org/10.1117/1.jnp.12.026018

47. Debasu ML, Riedl JC, Rocha J, Carlos LD. Li+ Role in Upconversion emission enhancement of (YYbEr)2O3 nanoparticle. Nanoscale 2018; 10 (33) :15799-15808. https://doi.org/10.1039/x0xx00000x

48. Basavegowda N, Mishra K, Thombal RS, Kaliraj K, Lee YR. Sonochemical green synthesis of yttrium oxide (Y2O3) nanoparticles as a novel heterogeneous catalyst for the construction of biologically interesting 1,3-thiazolidin-4-ones. Catalysis Letters 2017; 147: 2630-2639. https://doi.org/10.1007/s10562-017-2168-4

49. Kądziołka-Gaweł M, Czaja M, Dulski M, Krzykawski T, Szubka M. Impact of high temperatures on aluminoceladonite studied by Mössbauer, Raman, X-ray diffraction and X-ray photoelectron spectroscopy. Mineralogy and Petrology 2021; 115: 431-444. https://doi.org/10.1007/s00710-021-00753-z

50. Huang Q, Wang J, Sun Y, Li X, Wang X, Zhao Z. Gas-sensing properties of composites of Y-zeolite and SnO2. Journal of Materials Science 2018; 53: 6729-6740. https://doi.org/10.1007/s10853-018-2016-y

51. El Garah M, Touaibia DE, Achache S, Michau A, Sviridova E, Postnikov PS, Chehimi MM, Schuster F, Sanchette F. Data on nitridation effect of AlTiTaZrHf(-N) high entropy films by X-ray photoelectron spectroscopy. Data in Brief 2022;42:108241. https://doi.org/10.1016/j.dib.2022.108241

52. Tan D, Ma Z, Xu B, Dai Y, Ma G, He M, Jin Z, Qiu J. Surface passivated silicon nanocrystals with stable luminescence synthesized by femtosecond laser ablation in solution. Physical Chemistry Chemical Physics 2011; 13: 20255-20261. https://doi.org/10.1039/c1cp21366k

53. Xu D, Fan D, Shen W. Catalyst-free direct vapor-phase growth of Zn1-xCuxO micro-cross structures and their optical properties. Nanoscale Research Letters 2013; 8: 46. https://doi.org/10.1186/1556-276X-8-46

54. Liang YC, Wang CC. Surface crystal feature-dependent photoactivity of ZnO-ZnS composite rods via hydrothermal sulfidation. RSC Advances 2018; 8: 5063-5070. https://doi.org/10.1039/c7ra13061a

55. Karikalan N, Karthik R, Chen SM, Karuppiah C, Elangovan A. Sonochemical Synthesis of sulfur doped reduced graphene oxide supported CuS nanoparticles for the non-enzymatic glucose sensor applications. Scientific Reports 2017; 7: 2494. https://doi.org/10.1038/s41598-017-02479-5

56. Jin Z, Liu C, Qi K, Cui X. Photo-reduced Cu/CuO nanoclusters on TiO2 nanotube arrays as highly efficient and reusable catalyst. Scientific Reports 2017; 7: 39695. https://doi.org/10.1038/srep39695

57. Kaya EE, Unal F, Kazmanlı, K, Gürmen S. Fabrication and characterization of Yb-doped Y2O3 powders and thin films. International Journal of Materials Research 2020; 111 (7): 559 -566. https://doi.org/10.3139/146.111913

58. Unal F, Kaya F, Kazmanli K. Effects of dopant rate and calcination parameters on photoluminescence emission of Y2O3:Eu3+ phosphors: A statistical approach. Ceramics International 2019;45:17818-17825. https://doi.org/10.1016/j.ceramint.2019.05.353

59. Breviglieri ST, Cavalheiro ETG, Chierice GO. Correlation between ionic radius and thermal decomposition of Fe(II), Co(II), Ni(II), Cu(II) and Zn(II) diethanoldithiocarbamates. Thermochimica Acta 2000; 356: 79-84. https://doi.org/10.1016/S0040-6031(00)00465-2